Effects of wall conductivities on magnetoconvection in a cube

Hai-Tao Zhu,* Long Chen,* and Ming-Jiu Ni†
School of Engineering Science, University of Chinese Academy of Sciences, Beijing 101408, China

(Received 26 December 2023; accepted 14 March 2024; published 8 April 2024)

This research article delves into the natural convection of liquid metal in a three-dimensional cavity with varying magnetic fields and wall conductivities using direct numerical simulation. Two opposite sidewalls are heated/cooled, while the magnetic field is perpendicular to the main circulation. Our primary focus is on examining flows within the Grashof number, $\mathrm{Gr} \leqslant 10^8$, the Hartmann number, $\mathrm{Ha} \leqslant 400$, and the wall conductance ratio, $C_w = 0.01$–1. It is found that weakly conducting walls experience a significant enhancement in convection within a specific range of magnetic field strength, whereas highly conducting walls exhibit pronounced flow attenuation. The applied horizontal magnetic field alters the plume's topology and dynamics, generating a more coherent and energetic large-scale flow structure, while it weakens convection by consuming buoyant potential energy through Joule dissipation. This results in a competition between the rectifying effect and the damping effect to determine whether the magnetic field has a positive or negative feedback on heat transfer, with the quasi-two-dimensional state serving as a critical point. Additionally, varying wall conductivities transform the current distribution within the parallel layer, influencing the flow's response to changes in field strength. The formation of corner vortices can be considered by the curvature of the boundary layer that undergoes turning at corners. Furthermore, the effects of wall shear and plume transport on heat transfer are systematically investigated. The analysis reveals that while the plume area remains almost constant, the condensation of coherent structures facilitates greater horizontal heat transport per unit area of the plume, contributing significantly to the overall heat transfer enhancement. Finally, the computed Nusselt number Nu and Reynolds number Re can be correlated as functions of $\mathrm{Ha}/\mathrm{Gr}^{1/3}$. The critical conductance ratio referring to the complete suppression of convection conforms to the scaling of $2.31(\mathrm{Ha}/\mathrm{Gr}^{1/3})^{-5}$, where heat transfer occurs solely by thermal conduction once it exceeds this value.

DOI: 10.1103/PhysRevFluids.9.043701

I. INTRODUCTION

Convection subjected to an externally applied magnetic field, referred to as magnetoconvection (MC), holds significance not just in astrophysical [1] and geophysical [2] phenomena, but also in crucial engineering domains including liquid metal batteries [3], fusion reactor blankets [4], and crystal growth [5]. The magnetic field introduces flow anisotropy, leading to alterations in the flow structure contingent upon the magnetic field's orientation, strength, and additional boundary conditions. This suggests that magnetoconvection displays a broad spectrum of dynamic properties.

The standard paradigm for studying thermal convection is the Rayleigh-Bénard convection (RBC) [6–8], characterized by heating from the bottom and cooling from the top. When applying this temperature gradient along the vertical sidewalls rather than the top and bottom plates, a

*These authors contributed equally to this work.
†mjni@ucas.ac.cn

related yet distinctly different physical model is formulated. Batchelor referred to this system as a "differentially heated cavity" [9]. Since the horizontal heat transfer direction is orthogonal to the vertical buoyancy flux, it is also termed "vertical convection" (VC). Moreover, the large-scale dynamics [10,11], boundary layer [12,13], and global transport [14–16] in vertical convection have been extensively investigated, but the physical properties of its coupling to magnetic fields have not been fully revealed.

It is commonly accepted that the flow of electrically conducting fluid in a strong magnetic field is mainly controlled by the Lorentz force [17], with the resulting Joule dissipation causing a strong attenuation of the angular momentum perpendicular to the field lines, while the viscous effect is confined to an extremely thin boundary layer. In the core region, the flow aligns significantly with the field lines, and alterations in physical quantities along this direction are typically negligible. Under conditions of wall insulation [18], the two-dimensional equations can be obtained by averaging the equations of motion integrally along the field lines. The Lorentz force is expressed here as a linear term, regarded as the friction indirectly induced by shaping the Hartmann layer, i.e., the SM82 model [19]. This model and its subsequent extensions have been widely used in numerical simulations in the fields of magnetohydrodynamics (MHD) duct flow [20], thermal convection, and shear turbulence [21], and they have shown great superiority. However, if the boundary walls conduct currents, the validity of the quasi-two-dimensional (Q2D) model is compromised, leading to highly inaccurate velocity calculations for the side layer and necessitating three-dimensional simulations [22].

Therefore, aside from the magnetic field itself, it is significant to explore the potential influence of wall conductivity on convective motion. Hunt's pioneering work [23] indicated that in wall-conducting MHD duct flow, the velocity profile exhibits a flat core, an exponential boundary layer perpendicular to the magnetic field, and jets near the walls parallel to the magnetic field. The jets appear due to a specific current distribution that makes the side layers much less damped than the core, resulting in higher fluid velocity near the side walls.

Reflected in vertical convection, the research in question was initially inspired by Tagawa and Ozoe [24] with the numerical simulations in a conductive cavity. It is shown that a magnetic field applied perpendicular to the isothermal wall is more effective in suppressing convective motion than a parallel field. Di Piazza and Ciofalo [25] used the thin wall condition to deal with the potential boundary of the conducting walls, and the fine mesh required to resolve the Hartmann layer was replaced by an integral model. They found that increasing the wall conductance ratio will strengthen the square shape of the circulation cell, and there is a weak reverse flow in the core region, which may be related to the additional circulation center. Meanwhile, Gajbhiye and Eswaran [26] reported that the damping of convection by increasing wall conductivity is not continuous, but there is a threshold value of conductance ratio of about 10. In addition to the wall electric conduction, if the heat conduction in the solid domain is considered at the same time, the three-dimensional effect of flow will be much stronger [27]. Similar wall effects have also been observed in truncated conjugated cavities [28], and natural convection coupled with melting in the presence of an internal heat source can provide a reference for further comprehension [29]. These intriguing dynamic properties have captured our attention, yet limited discussion has been devoted to the underlying physical mechanisms associated with the conducting wall. Furthermore, a systematic analysis of the quantitative relationship between global transport and dimensionless parameters remains largely unexplored. While an extension of the unified theory of thermal convection scaling [30] to MC has recently been proposed [31], this discussion is also grounded on insulating walls.

The preceding contemplations prompt us to reexamine vertical convection within the conducting walls across a wider range of parameters, rather than confining our analysis to the extremes of insulation or complete conductivity. Our present research aims to explore the following inquiries:

(i) How does the change in wall conductance ratio affect the vertical convection system?

(ii) For low-Pr fluids, how do we delineate the evolution of corner vortices under the magnetic field, as a flow characteristic of cavity?

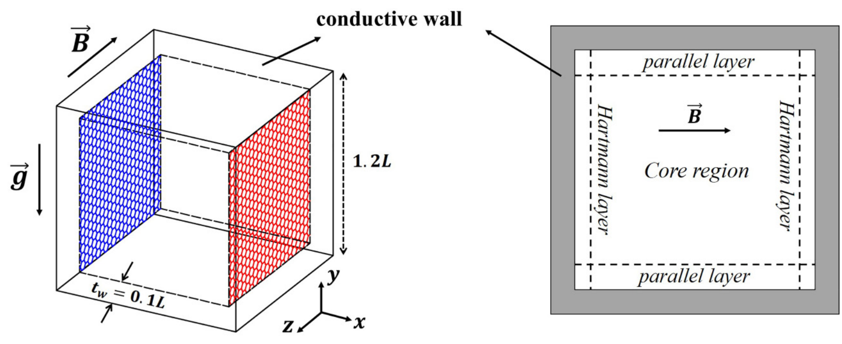

(a) 3D cavity (b) yz-plane

FIG. 1. Schematic diagram of the studied physical model.

(iii) Can we establish empirical formulas correlating the Nusselt and Reynolds numbers with the Hartmann and Grashof numbers for different wall conductivities?

(iv) Is there a rectification effect akin to the magnetic field observed within insulating walls [32] in the case of conducting walls? Does it lead to an intensified convective heat transfer? What are the specific mechanisms involved in this process, and what factors primarily influence it?

The remainder of this paper is organized as follows. In Sec. II, we outline the numerical model, the algorithm, and the setup of the simulations. Section III A discusses the effect of wall conductivity on the flow organization by analyzing the Lorentz force and current distribution. In Sec. III B, we describe the temperature field, focusing on the thermal stratification phenomenon characterizing the convective intensity and the evolution of the corner structure. Section III C presents the result regarding how the global Nusselt and Reynolds numbers respond to the values of Hartmann numbers, Grashof numbers, and wall conductance ratio (C_w), and it explores the exact physical mechanism behind the nonmonotonic change in heat transfer. Finally, we offer concluding remarks in Sec. IV.

II. MODEL AND FORMULATION

A. Governing equations

The study focuses on natural convection in a three-dimensional cavity with a specific wall thickness, as illustrated in Fig. 1(a). The cavity is filled with liquid metal having a Prandtl number of 0.025. The width of the fluid domain is denoted by L, and the wall thickness is $0.1L$. The vertical inner walls at the left and right sides have a temperature difference, and an orthogonal magnetic field is applied to the temperature gradient. Notably, unlike the conventional adiabatic horizontal wall, a linear transition in temperature distribution from cold to hot is employed for the top and bottom walls, although not indicated on the schematic diagram. This condition helps to enhance turbulence levels in the flow [33], thereby enabling the capture of richer flow phenomena within a limited range of parameters. In addition, the difference in electrical conductivity between the solid walls and the fluid is characterized by the wall conductance ratio ($C_w = \sigma_w t_w/\sigma L$), which is primarily considered in the range of 0.01–1 in this study.

The cross-section in the yz-plane, as shown in Fig. 1(b), includes different layers of the flow. The Hartmann layer, with a thickness of L/Ha, is perpendicular to the magnetic field, and the parallel layer, with a thickness of $L/\sqrt{\mathrm{Ha}}$, is parallel to the magnetic field. These different layers have different flow characteristics and play a crucial role in the overall heat transfer process. The core region is usually characterized by the formation of large-scale vortex and recirculation zones, which are responsible for mixing the fluid and transporting heat.

The liquid metal in question is deemed an incompressible Newtonian fluid. The Boussinesq assumption is applied to express the buoyancy force, which results from density change, as a linear function of temperature. In the context of the liquid metal flow within practical engineering applications such as fusion reactors, the induced magnetic field does exist, but it is much smaller than the applied magnetic field ($\mathrm{Re}_m = uL/\eta \ll 1$), and it can be neglected once it appears together with the applied one. Additionally, compared to heating from thermostatic walls, the contribution of Joule dissipation can be ignored [34]. These considerations led to the establishment of the following three-dimensional dimensionless governing equations:

$$\nabla \cdot \boldsymbol{u} = 0, \tag{1}$$

$$\frac{\partial \boldsymbol{u}}{\partial t} + \boldsymbol{u} \cdot \nabla \boldsymbol{u} = -\nabla p + \nabla^2 \boldsymbol{u} + \mathrm{Ha}^2(\boldsymbol{j} \times \boldsymbol{B}) + \mathrm{Gr} T e_y, \tag{2}$$

$$\boldsymbol{j} = -\nabla \phi + \boldsymbol{u} \times \boldsymbol{B}, \tag{3}$$

$$\nabla \cdot \boldsymbol{j} = 0, \tag{4}$$

$$\frac{\partial T}{\partial t} + \boldsymbol{u} \cdot \nabla T = \frac{1}{\mathrm{Pr}} \nabla^2 T, \tag{5}$$

where $\boldsymbol{u}$, $\boldsymbol{j}$, $\boldsymbol{B}$, T, and ϕ stand for the velocity, current density, magnetic field, temperature, and electric potential scaled by the characteristic values ν/L, $\sigma \nu B_0/L$, B_0, ΔT, and νB_0, respectively.

The above equations feature three dimensionless parameters that determine the fluid behavior: the Prandtl, Grashof, and Hartmann numbers,

$$\mathrm{Pr} = \frac{\nu}{\kappa}, \quad \mathrm{Gr} = \frac{g\beta \Delta T L^3}{\nu^2} \quad \text{and} \quad \mathrm{Ha} = B_0 L \sqrt{\frac{\sigma}{\rho \nu}},$$

where Ha denotes the ratio of electromagnetic force to viscous force. The current study considers cases with $\mathrm{Gr} \leqslant 10^8$ and $\mathrm{Ha} \leqslant 400$, within which range the three-dimensional instability can be observed while turbulence is not yet established.

B. Boundary conditions

The boundary conditions employed to solve this conjugate problem are expressed as follows:

$$\boldsymbol{u} = 0, \quad x = \pm 0.5,\ y = \pm 0.5,\ z = \pm 0.5, \tag{6}$$

$$T = \pm 0.5, \quad x = \pm 0.5, \tag{7}$$

$$T = x, \quad y = \pm 0.5, \tag{8}$$

$$\partial T/\partial y = 0, \quad z = \pm 0.5, \tag{9}$$

$$\partial \phi/\partial n = 0, \quad x = \pm 0.6,\ y = \pm 0.6,\ z = \pm 0.6. \tag{10}$$

To couple the solutions across all interfaces between fluid and solid regions, the continuous distribution of electric potential and wall-normal component current density is ensured: $\phi_f = \phi_s$ and $j_{n,f} = j_{n,s}$, where the subscripts f and s denote the fluid region and the solid region, respectively. The temperature and heat flux at the interfaces between fluid and solid regions must satisfy the continuous boundary conditions as well, i.e., $T_f = T_s$ and $q_{n,f} = q_{n,s}$, which ensure that the solutions are coupled properly.

TABLE I. Grid node parameters and sensitivity analysis.

	$N_{\text{fluid},x}$	$N_{\text{fluid},y}$	$N_{\text{fluid},z}$	N_{solid}	$\overline{\text{Nu}}$	$\langle U_y \rangle$(max)
$G1$	60	60	60	12	4.7345	3.919×10^3
$G2$	80	80	80	15	4.7453	3.948×10^3
$G3$	100	100	100	18	4.7484	3.956×10^3

C. Numerical algorithm

The numerical simulations presented in this paper utilize the MHD finite-volume solver "MHD-UCAS" [35,36], with second-order accuracy in both time and space. The projection algorithm is employed to address the coupled pressure-velocity field. Initially, the predicted step velocity is derived at the mesh center by solving the momentum equation based on the pressure obtained in the prior iteration. Subsequently, the anticipated velocity flux on the mesh surface is computed as the source term for the pressure Poisson equation, which resolves the pressure difference, updating both pressure and velocity. The potential Poisson equation is then solved to acquire the potential, and the current density at the grid interface is determined through the consistent and conservative scheme. The current at the grid center is derived through conservation interpolation, facilitating the computation of the Lorentz force. This obtained Lorentz force is incorporated into the momentum equation as a source term to compute the velocity and pressure at the next time step. Typically, two iterations are necessary for the prediction step before solving the potential Poisson equation. The equations employ second-order implicit backward differences for the time term, while the convective and diffusive terms utilize center difference formats.

The efficacy of this numerical code has been extensively validated for both laminar and turbulent flows [21,37]. To guarantee computational stability in simulating unsteady flows, the present study is executed with a constant time step size, thereby ensuring that the maximum Courant number remains small enough ($\text{Co}_{\text{max}} = u_f n_f \Delta T/|d| \leqslant 0.3$). Furthermore, we have adopted a uniform convergence criterion of 10^{-6} for the velocity, pressure, temperature, and electric potential.

D. Grid independence study

To accurately capture the jet patterns present in the side layers and the possible complex structures while considering acceptable computational cost in the study of MHD vertical convection, we have employed a high-resolution mesh with nonuniform cell clustering in the boundary layers. For grid independence analysis, we have utilized three distinct grids ($G1$, $G2$, $G3$) with varying degrees of coarseness. Table I presents the distribution of specific nodes and corresponding test results. Notably, the discrepancy between $G2$ and $G3$ is reduced to a mere 0.34%, compared to the 1.37% difference between $G1$ and $G3$. Figure 2(a) illustrates the grid independence result, leading to the conclusion that $G2$ strikes the optimal balance between sufficient resolution and computational cost in calculations.

Finally, for a complete test of the numerical methods and grids used in this paper, we run test cases for comparison with published results. As illustrated in Fig. 2(b), the Nusselt numbers obtained for $\text{Pr} = 0.01$ and $C_w = 0.01$ show a strong correlation with the data of Gajbhiye and Eswaran [26]. This concordance substantiates the numerical simulation's accuracy presented in this study.

III. RESULTS AND DISCUSSION

A. Wall effects on the velocity

Due to the buoyancy effect, the fluid near the low-temperature wall and the high-temperature wall moves downward and upward, respectively, giving rise to two high-pressure regions at the lower left and upper right, as illustrated in Fig. 3(b). This pressure gradient drives the horizontal

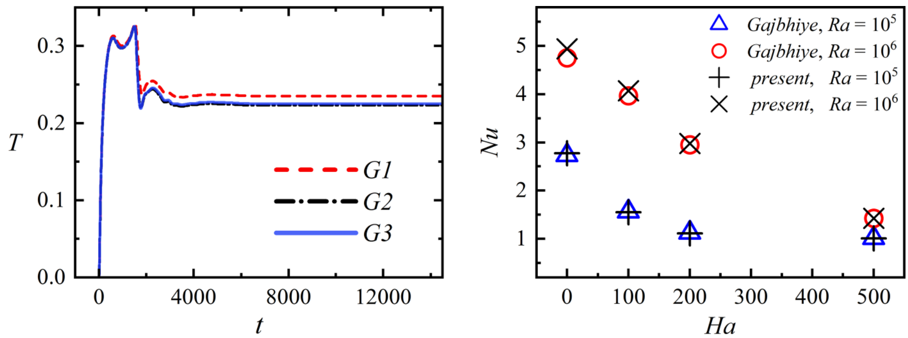

(a) Grid sensitivity study

(b) Nusselt numbers verification with Gajbhiye and Eswaran [26]

FIG. 2. (a) Temperature monitoring for $\mathrm{Gr} = 10^8, \mathrm{Ha} = 200$, and $C_w = 0.1$ at the probe location $(0.45, 0, 0)$. (b) Comparison of Nu between Gajbhiye and Eswaran [26] and the present simulations at $\mathrm{Pr} = 0.01$ and $C_w = 0.01$.

motion of the fluid, ultimately leading to the formation of a large-scale circulation structure, as reported in Ref. [27].

In the scenario of low-conducting walls, the velocity profiles (Fig. 4) reveal a notable increase in the peak with the increment of Ha, signifying an enhancement in flow intensity. Concurrently, the jet width diminishes progressively, and the "overshoot" phenomenon [38] at the outer edge of the boundary layer becomes distinctly observable. Alterations in the streamlines (Fig. 5) exhibit a gradual suppression of intricate and chaotic three-dimensional structures. Nonetheless, the influence of the Lorentz force on the overall flow field remains limited, while corner vortices persist around the cavity. Conversely, for high-conducting walls, a rapid decline of approximately 25% in jet velocity occurs with each increase of 100 units in Ha. Three-dimensional streamlines are absent, and the corner vortices transform from an initial distribution around all sides to retaining two distinct flow separation structures in the lower-left and upper-right corners before eventually being completely suppressed.

From the depiction of flow imagery, we can extract two pivotal inquiries: first, the mechanism by which the magnetic field enhances convection in weakly conductive walls while inducing a stark

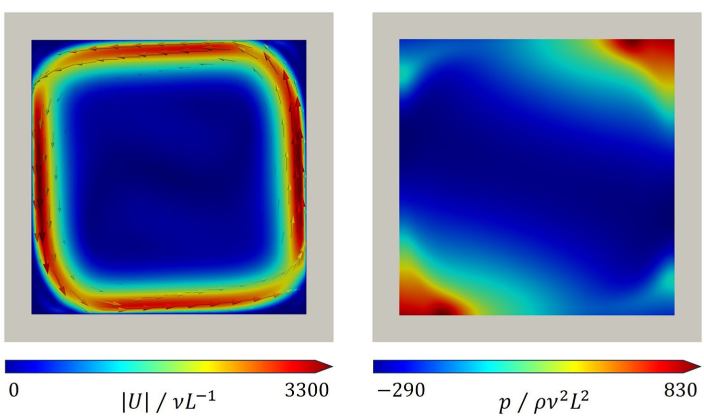

(a) Velocity distribution

(b) Pressure distribution

FIG. 3. Buoyant convection for $\mathrm{Gr} = 3 \times 10^7$, $\mathrm{Ha} = 200$, and $C_w = 0.1$.

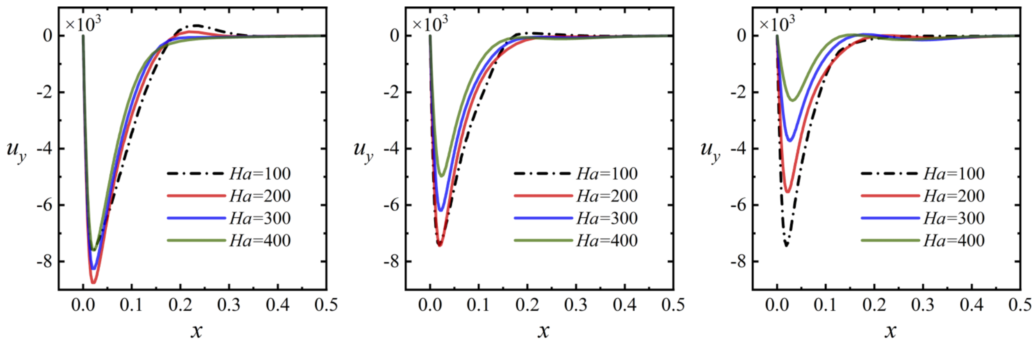

(a) $C_w = 0.01$ (b) $C_w = 0.1$ (c) $C_w = 1$

FIG. 4. The distribution of the mean vertical velocity along the x-axis near the cold wall for $\mathrm{Gr} = 10^8$.

decline in flow for highly conductive walls; second, the reasons behind the divergent sensitivity to magnetic field variations exhibited by walls of different conductivities.

The elucidation of the first issue can be contemplated within the framework of the visualized vortex structure in Fig. 6: at $C_w = 0.01$ and $\mathrm{Ha} = 100$, numerous diminutive vortex structures perpendicular to the primary vortex manifest on the surface of the main circulation. It is discernible that the fragments resulting from the disruption of the side vortex are stretched and ensnared onto the surface due to the convoluted suction effect exerted by the primary vortex, inclusive of its inherent deformation. This process engenders a vigorously oscillating three-dimensional flow structure. With

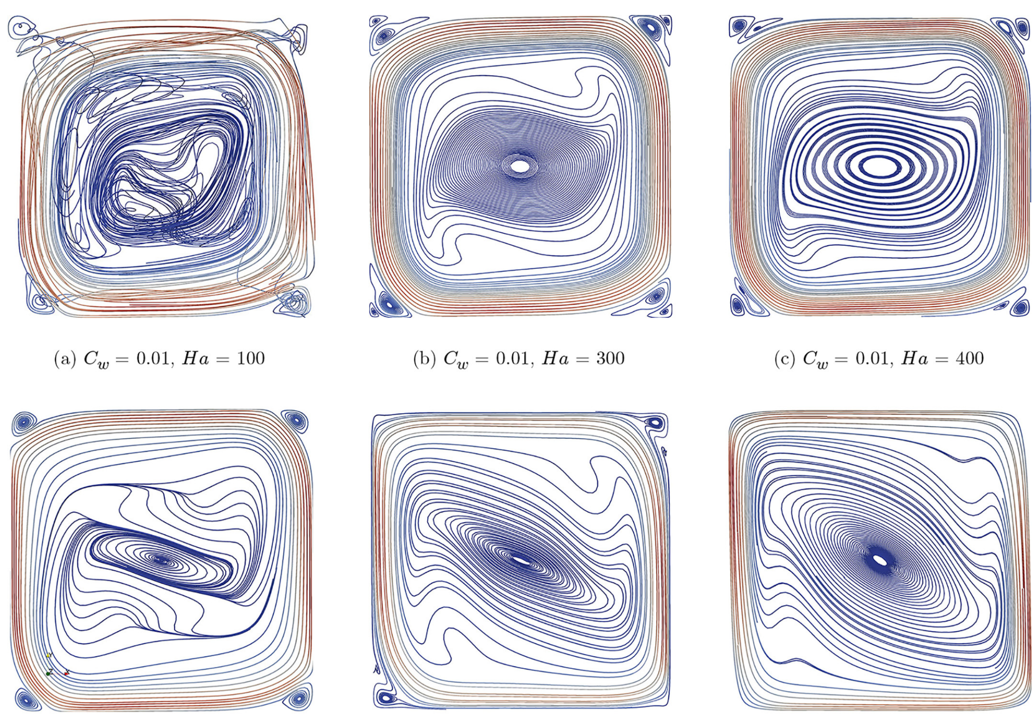

(a) $C_w = 0.01$, $Ha = 100$ (b) $C_w = 0.01$, $Ha = 300$ (c) $C_w = 0.01$, $Ha = 400$

(d) $C_w = 1$, $Ha = 100$ (e) $C_w = 1$, $Ha = 300$ (f) $C_w = 1$, $Ha = 400$

FIG. 5. Streamline plots at the midplane $z = 0$ for $\mathrm{Gr} = 8 \times 10^7$.

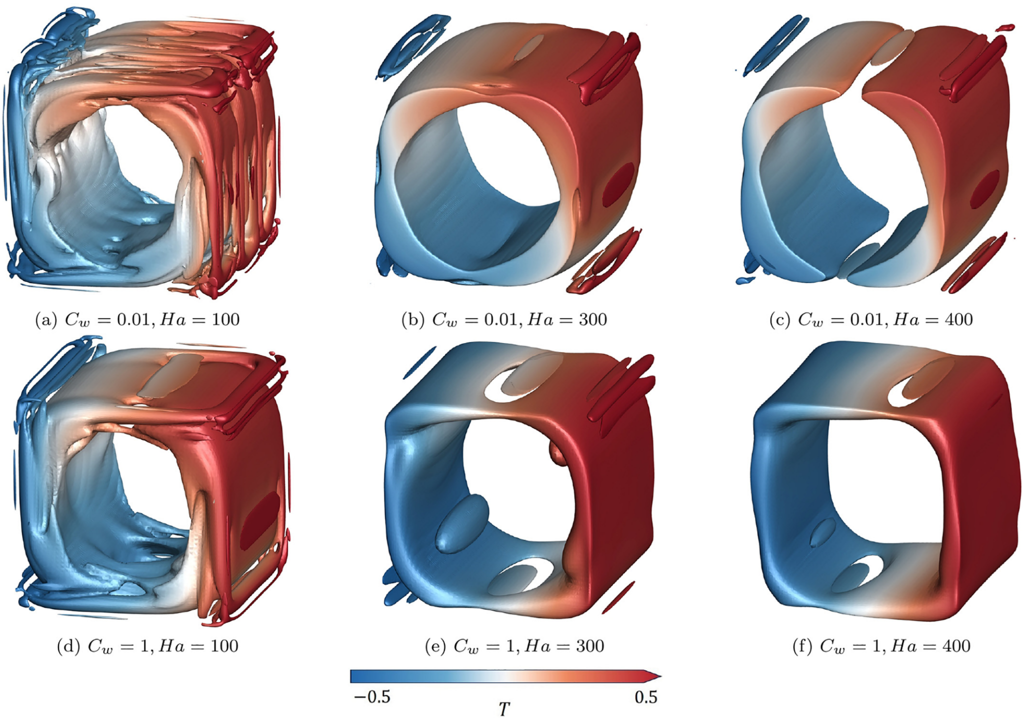

FIG. 6. The isosurface of $Q_{3D} = 0.5 * (||A||_F^2 - ||S||_F^2)$ (the second invariant of the velocity gradient tensor, S is a symmetric tensor and A is an antisymmetric tensor) represents the roll structures for $\mathrm{Gr} = 8 \times 10^7$, colored by local temperature.

the augmentation of the magnetic field, the flow evolves from 3D to Q2D. The side vortices are elongated along the magnetic field lines and no longer have significant interruptions, thereby exhibiting a markedly reduced interaction with the central vortex. The surface is rendered smoother, while the intricate structure along the axial direction is restrained by the magnetic field. This contributes to the formation of a more coherent and improved self-organized large-scale circulation (LSC). This process adheres to the inverse energy cascade observed in classical 2D turbulence, where energy progresses from the forcing scale up to large-scale structures [39]. Specifically, the magnetic field bolsters the system-size flow by directing the energy of the small-scale vortex upwards to the main vortex. As the coherence of the global flow intensifies, the thermal convection system attains the so-called "optimal state." The definition of this state has garnered multiple interpretations within RBC. Lim [40] posits that the optimal enhancement can be understood through the intersection of the thermal and momentum boundary layers. Vogt [41] suggests that the maximum velocity might occur when the fluid's potential buoyancy energy transforms entirely into kinetic energy, i.e., the theoretical free-fall limit. If the magnetic field continues to increase after reaching the optimum, the Hartmann braking, indicative of the magnetic damping effect, undergoes further reinforcement. However, beyond this juncture, the flow coherence cannot continue to improve, and the convective strength diminishes as dissipation increases. As depicted in Fig. 6(d), in scenarios involving highly conductive walls, the presence of coherent side vortices, aligned strictly parallel to the field direction, and the regular main vortex surface, both indicate that the flow has already reached an approximate Q2D state, even at the weakest magnetic field. Subsequently, any further enhancement of the magnetic field would solely result in escalated dissipation within the Hartmann layer, imposing a robust damping effect on the flow. (A more detailed quantitative analysis of the flow coherence is given in Sec. III C.)

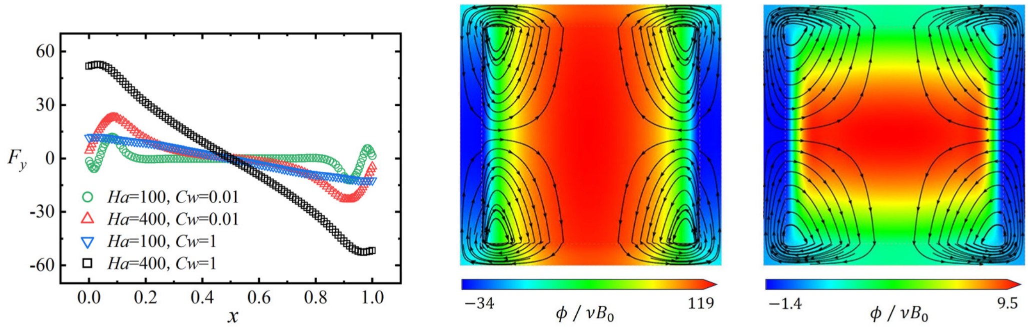

(a) Lorentz force in the vertical direction.

(b) Electric current and potential at mid xz-plane $y = 0$. (left) $C_w = 0.01$ (right) $C_w = 1$

FIG. 7. The distribution of vertical Lorentz force along the x-axis and electric current in solid-fluid domain for $\mathrm{Gr} = 3 \times 10^7$.

Regarding the second inquiry, it is logical to approach the investigation of the flow mechanism through the lens of force, as illustrated in Fig. 7(a). In the case in which $C_w = 0.01$, augmenting the magnetic field yields no substantial alteration to the Lorentz force. The force peak is focused at both extremities adjacent to the sidewall, with a restricted damping effect on the core region. Conversely, for $C_w = 1$, varying Ha values result in a relatively significant disparity in F_y, which is inclined to distribute linearly along the x-direction. At higher Ha, convective motion is considerably suppressed.

Figure 7(b) illustrates the distribution of induced currents for different wall conductivities, which can be employed to elucidate the distinction in F_y. For $C_w = 0.01$, a majority of the currents traverse the side layer and form loops without permeating the wall, resulting in current vectors primarily aligned parallel to the magnetic field in the side layer. Consequently, even if the magnetic field intensity increases, it has a limited impact on the Lorentz force. When $C_w = 1$, the currents within the side layer penetrate the interface perpendicularly into the sidewall, which corresponds to current vectors predominantly perpendicular to the magnetic field. This indicates a complete conversion to the Lorentz force, leading to a more pronounced damping effect.

In addition, employing the initial dimensionless governing equations allows us to estimate the horizontal flow rate within the conducting cavity. From the above analysis, it is evident that the convection demonstrates a Q2D pattern that remains consistent along the z-direction, particularly observed when the magnetic field strength is high or the conductivity is substantial, and we focus on the flow in the plane perpendicular to B. To derive the vorticity equation, we take the curl of Eq. (2) and examine its field-aligned component ω_z, which can be written as

$$\left(\nabla \times \frac{\partial \mathbf{u}_\perp}{\partial t}\right)_z = \nabla^2 \omega_z + \mathrm{Gr}\frac{\partial T}{\partial x} + \mathrm{Ha}^2 \frac{\partial j_z}{\partial z}. \tag{11}$$

When $\mathrm{Ha} \gg 1$, the flow is primarily governed by the balance between the buoyancy and Lorentz force terms, while the inertial and viscous terms are disregarded. During this phase, convective effects become less significant, leading to an approximately linear horizontal temperature distribution,

$$-\frac{\partial j_z}{\partial z} = \frac{\partial^2 \phi}{\partial z^2} = \frac{\mathrm{Gr}}{\mathrm{Ha}^2}\frac{\partial T}{\partial x} \approx \frac{\mathrm{Gr}}{\mathrm{Ha}^2}. \tag{12}$$

Integrating Eq. (12) along field lines provides the potential distribution and its mean value over z as

$$\phi = \phi_0 + \frac{\mathrm{Gr}}{2\mathrm{Ha}^2}\left(z^2 - \frac{1}{4}\right) \quad \text{and} \quad \overline{\phi} = \phi_0 - \frac{\mathrm{Gr}}{12\mathrm{Ha}^2}, \tag{13}$$

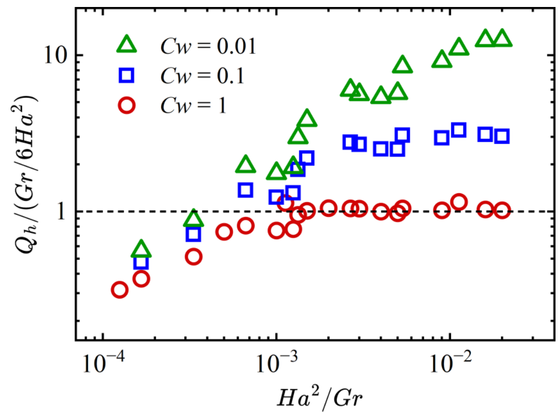

FIG. 8. Flow rate estimation of the horizontal jet in the cavity.

where ϕ_0 is the potential at the Hartmann wall, and the actual potential is not uniformly distributed along the field lines. The dimensionless flow estimate for the horizontal jet can be written as

$$Q_h = 2\int_z \int_{\delta_{sh}} u\, dy\, dz = -\int_{\delta_{sh}} \frac{\partial \overline{\phi}}{\partial y}\, dy = \overline{\phi_\delta} - \overline{\phi_w} = \frac{\mathrm{Gr}}{6\mathrm{Ha}^2}. \tag{14}$$

For perfectly conducting walls, $\overline{\phi_w} = 0$. Figure 8 illustrates the ratio between the actual statistical flow rate and the theoretically calculated counterpart for each parameter. In cases of high conductivity ($C_w = 1$), the theoretical predictions align well with the actual flow once the magnetic field reaches a certain strength, as assumed during the derivation process. However, for low C_w values, the temperature profile shift caused by intense convection becomes significant, i.e., $\partial T/\partial x \neq$ const. Consequently, the potential at the side layer's edge becomes spatially correlated, leading to error in estimating the average potential. As stated in the previous analysis of currents, the magnetic field's impact on flow is overestimated for low C_w, causing the actual flow rate to exceed the theoretical prediction significantly.

To acquire a deeper comprehension of the impact of conductive walls on the dimensionality of natural convection, we will investigate the spanwise distribution of relevant physical quantities at the peak position of the jet. Remarkably, as C_w increases, the induced current components generated by both the potential gradient and the fluid motion decrease [Fig. 9(a)], while the actual current generated by the difference between the two escalates ($j_x = u_y B_z - \partial\phi/\partial x$). The velocity disparity between the wall vicinity and the core region diminishes, indicating that the three-dimensional feature attributed to the no-slip boundary of the Hartmann wall is attenuated. The distribution of the Lorentz force within the core region and the Hartmann layer, as depicted in Fig. 9(b), presents several intriguing properties. The damped Lorentz force in the core region, corresponding to the highly conductive wall, exhibits a more evenly dispersed alignment along the spanwise direction, coupled with a heightened amplitude. The curvature displayed by each F_y profile generally conforms to the parabolic distribution of the current component. It is noteworthy that a driving Lorentz force that is an order of magnitude larger compared to the core region occurs within the Hartmann layer, which is particularly evident at the low-conducting walls. The current distribution in the vicinity of the Hartmann wall gives the answer: the currents tend to form loops through the Hartmann layer, resulting in a phenomenon of current accumulation, thereby generating an exponentially increasing velocity distribution within this layer. However, the potential gradient exhibits smooth variation and consistently remains significantly larger than the motional current within the Hartmann layer. Conversely, in the context of the high-conductivity wall, the current consistently traverses through the Hartmann layer, permeates into the solid domain, and completes a circuit at the corners of the

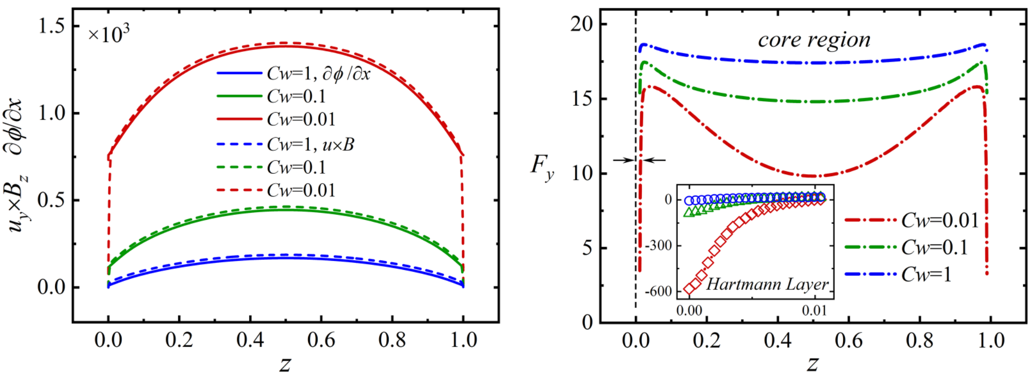

(a) $u_y B_z$ and $\partial\phi/\partial x$ (b) Vertical Lorentz force

FIG. 9. The spanwise distribution of physical quantities at the peak of jet for $\mathrm{Gr} = 10^7$ and $\mathrm{Ha} = 400$.

fluid-solid junctions. In this scenario, the current density within the fluid domain remains relatively diminished, without the manifestation of a prominently driven Lorentz force. It is crucial to highlight that despite the relatively minor magnitude of the spanwise Lorentz force within the core region in contrast to the Hartmann layer, its impact on both convective intensity and velocity profiles remains pivotal, and the seemingly modest lift of the high conductive wall compared to the low conductive wall is significant in attenuating the jet amplitude.

B. Wall effects on the temperature

In this section, the investigation focuses on elucidating the influence of wall effects specifically on temperature-correlated physical fields. First, the time series of temperature fluctuations, acquired in the vicinity of the thermal boundary layer adjacent to the hot wall, are presented in Fig. 10. The analysis is centered around fixed $\mathrm{Gr} = 1 \times 10^8$ and $\mathrm{Ha} = 100$, exploring the impact of varying wall conductivity on the statistical characteristics of MHD thermal convection. Additionally, the case without magnetic field is included as a reference. In the baseline scenario with $\mathrm{Ha} = 0$, the temperature signal displays the highest amplitude and showcases random fluctuations. The corresponding power spectral density (PSD) exhibits noise across the frequency spectrum, conforming to the thermal energy spectra characteristic of fully developed thermal turbulence. This spectrum includes a $-5/3$ slope in the inertial-convective subregion and a $-17/3$ slope in the inertial-conducting subregion [42], which aligns with the established scale often utilized in experimental determinations of the thermal turbulence state [43,44].

Upon application of a magnetic field under insulated wall conditions ($C_w = 0$), the amplitude of temperature fluctuations experiences some suppression, although high-frequency components and sharp peaks persist. In cases of weak wall conductivity ($C_w = 0.01$), the substantial reduction of high-frequency oscillation results in a flow state characterized by low-frequency chaotic oscillation. With a further increase in wall conductivity, fluctuations transition to quasiperiodic oscillations of reduced power until they ultimately cease entirely. Importantly, all temperature PSDs manifest prominent peaks representing the dominant oscillatory frequency of the system, f_{OS}. Drawing from previous research, we compare the timescale of a convective vortex overturning cycle to f_{OS}. Estimates of the overturning frequency f_{TO} are derived using circular paths within the cavity, with the maximum mean velocity. The dotted lines in the PSDs denote estimates of the overturning frequency, closely aligning with the oscillatory frequency, affirming the coherence of the large-scale flow structure in the context of vertical convection.

Figures 11 and 12 provide visualization of the temperature field. For low C_w, the influence of magnetic field variations is relatively minor, always with thin thermal boundary layers and a

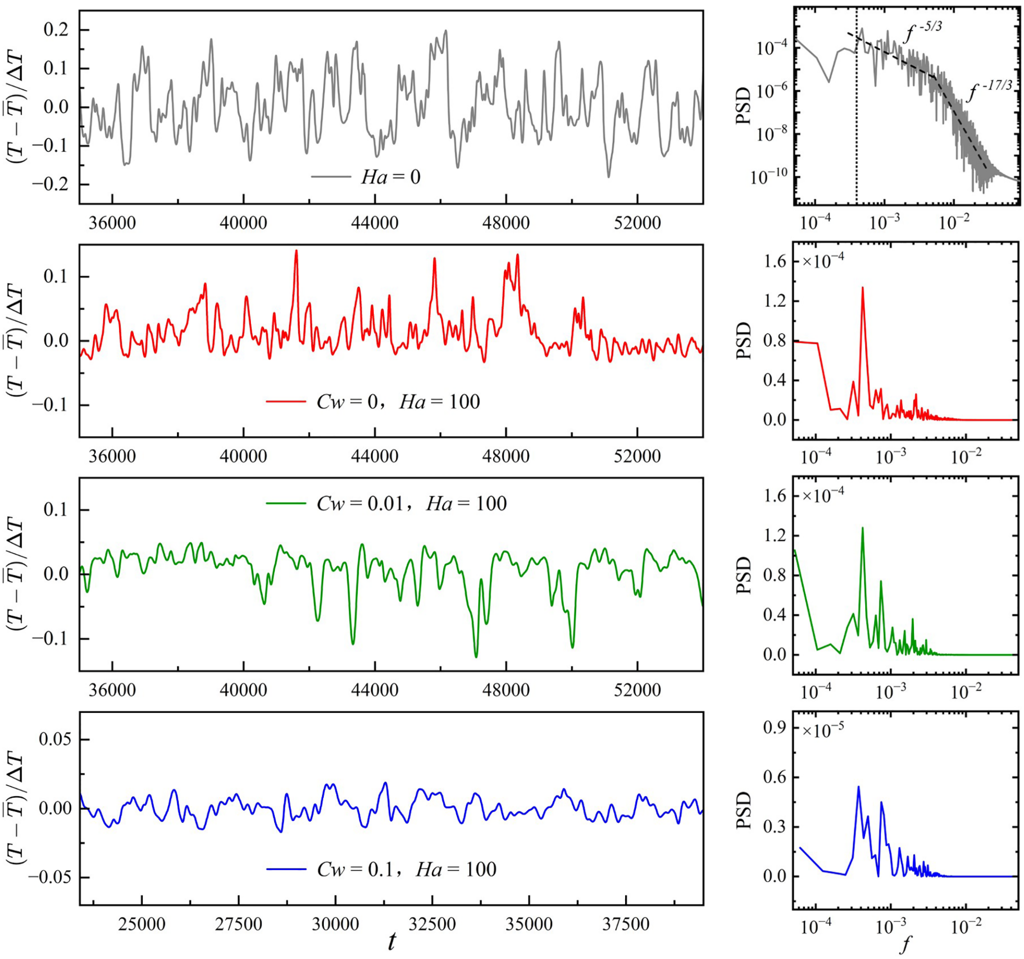

FIG. 10. Time series of temperature fluctuations monitored at the thermal boundary layer and the PSD for $\mathrm{Gr} = 1 \times 10^8$.

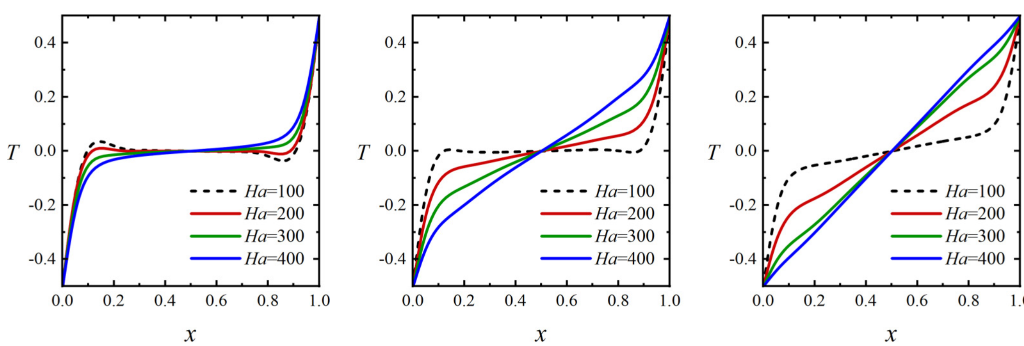

(a) $C_w = 0.01$ (b) $C_w = 0.1$ (c) $C_w = 1$

FIG. 11. The distribution of the mean temperature along the x-axis for $\mathrm{Gr} = 10^8$.

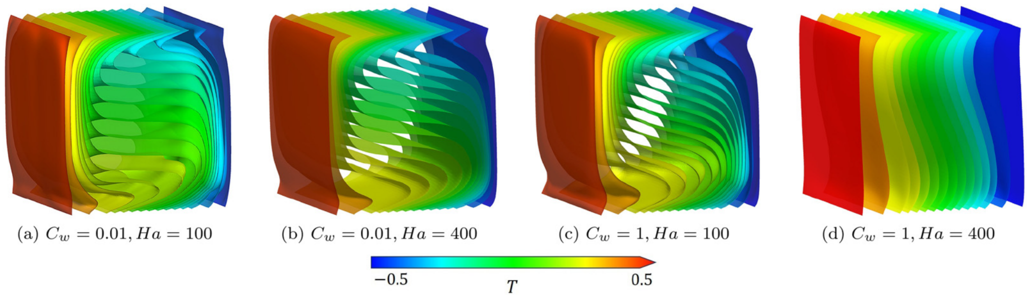

FIG. 12. The isothermal surface inside the fluid zone for $\mathrm{Gr} = 8 \times 10^7$.

well-mixed bulk region. The temperature distribution does not exhibit a monotonic rise from $T = -0.5$ at the cold wall to $T = 0$ in the bulk due to stable thermal stratification, causing an overshoot phenomenon in the temperature profile. Despite the diminished fluctuations in the temperature isosurfaces along the magnetic field direction, the three-dimensional flow characteristics remain apparent. Conversely, for high C_w, distinct current distributions induce temperature profiles that exhibit greater sensitivity to changes in Ha. The vertical thermal stratification gradually diminishes, indicating that the convective motion is strongly suppressed. The nearly oblique distribution of isothermal surfaces also depicts a stable Q2D flow.

The variations of the thermal stratification level can be quantified using the mean stratification parameter denoted S_θ, which is defined as the time-averaged nondimensional vertical temperature gradient at the center [45]:

$$S_\theta = \langle (L/\Delta T)/(\partial T/\partial y)_c \rangle_t. \tag{15}$$

As illustrated in Fig. 13, the stratification parameter values for all simulations can be transformed into a single curve via the parameter $\mathrm{Ha/Gr}^{1/2}$, which is essentially equivalent to the parameter combination Q/Gr commonly used in MC, where $Q = \mathrm{Ha}^2$ is the Chandrasekhar number. These three curves reveal distinct degrees of nonmonotonic variation trends. Here, $\mathrm{Ha/Gr}^{1/2}$ can be regarded as the relative magnitude of Lorentz force and buoyancy force, while S_θ can gauge the changes in the bulk temperature profile shape, indirectly reflecting the strength of convective motions. The apex of S_θ delineates the interval of Lorentz force enhancement and suppression on thermal convection in the core region. When $C_w = 0.01$, the alteration of S_θ is relatively uniform,

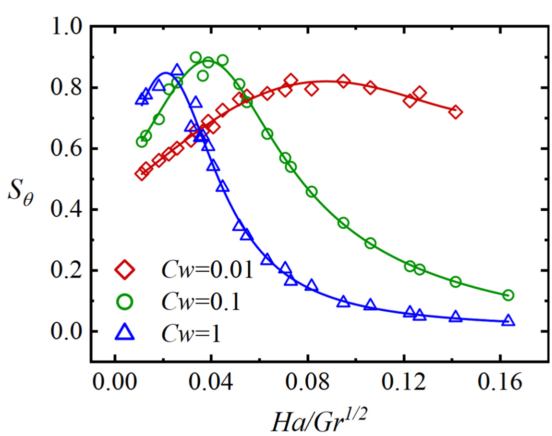

FIG. 13. The evolution of stratification parameter S_θ vs $\mathrm{Ha/Gr}^{1/2}$.

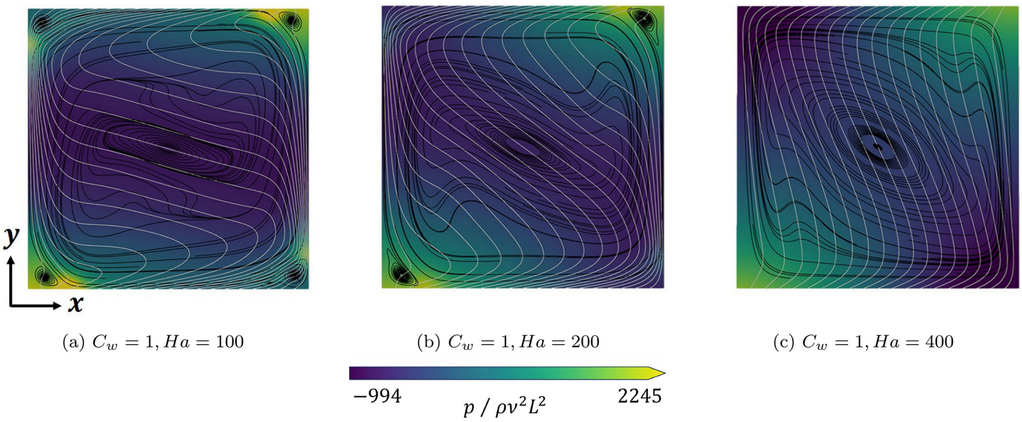

FIG. 14. Contours of pressure distribution with streamlines (black lines) and isothermals (white lines) at the midplane $z = 0$ for $\mathrm{Gr} = 8 \times 10^7$.

and the overall improvement of thermal stratification prevails. When $C_w = 0.1$ and 1, following a brief phase of enhancement interval, the vertical stratification generated by thermal convection decays rapidly. The transition to heat conduction leads to horizontal stratification, following the temperature distribution shown in Fig. 12(d).

As previously discussed, stable thermal stratification can induce both overshoot and undershoot phenomena within the vertical boundary layer [38]. In the vicinity of the heated wall, for instance, when the fluid ascends vertically, the heat transfer rate from the wall to the outer boundary layer is insufficient to maintain temperature synchronization with the exterior. Consequently, a cooler fluid relative to the core emerges, descending and separating from the horizontal wall as it passes through the corners, forming loops. However, in low-Pr fluids, the higher heat diffusion coefficient leads to shorter survival times for localized hot and cold plumes [46], resulting in a smoother temperature field overall. The isotherms depicted in Fig. 14 indicate minimal overshooting and undershooting in the corner region, except at the midheight, which relates to the fully thermally conductive boundary, in contrast to the adiabatic horizontal boundary. The extension of cold (hot) fluids downstream from the vertical wall diminishes as Ha increases, and the corner vortices surrounding them dissipate entirely after being retained at the lower-left and upper-right positions. Additionally, the locations of the corner structure correlate closely with the pressure distribution. Localized high pressure stems from the geometrically restricted turning of the vertical boundary layer into the horizontal boundary layer. Generally, thinner boundary layer thicknesses facilitate more pronounced transitions and the formation of flow-separated structures. Hence, we quantify both horizontal and vertical boundary layer thicknesses using spatiotemporally averaged velocity profiles ($\langle\overline{u_y}\rangle_{yz}$, $\langle\overline{u_x}\rangle_{xz}$), and we compare these measurements to the actual flow states.

As depicted in Fig. 15, the horizontal boundary layer thickness generally exceeds the vertical boundary layer thickness, and the trend of δ_u with increasing magnetic field is not consistent. At small Gr numbers, δ_u decreases monotonically with increasing magnetic field. During this phase, the damping effect of the Lorentz force takes precedence, causing δ_u to approach the scaling of the side layer thickness, $\sim 1/\sqrt{\mathrm{Ha}}$. And this decline occurs more rapidly in the case of highly conductive walls. At larger Gr numbers, the main circulation is enhanced due to the rectification effect of the magnetic field, and δ_u increases slightly. But for high C_w, this exists only in the weak magnetic field, presenting a nonmonotonic variation. Moreover, the relative magnitudes of the two boundary layer thicknesses exhibit a certain degree of association with the corner vortex configurations. In the phase diagrams shown in Fig. 16, we plot the corner vortex distribution for each parameter in conjunction with the boundary layer thickness information. The different symbols used in the diagrams serve as indicators: squares denote the presence of four corner vortices in the main circulation plane,

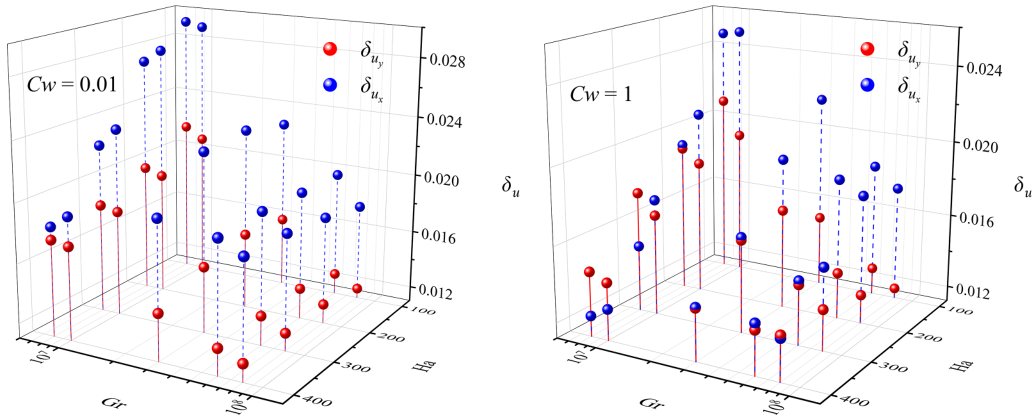

FIG. 15. Horizontal and vertical boundary layer thicknesses calculated using surface-time-averaged velocity profiles for $C_w = 0.01$ and 1 [$\delta_u = U/(d\bar{u}/dx|_{\text{wall}})$].

circles represent solely two vortices on the lower-left and upper-right sides, and triangles signify the absence of corner structures. Additionally, these symbols are color-coded based on the ratio of horizontal to vertical boundary layer thickness. Notably, regardless of conductivity, when the ratio between horizontal and vertical boundary layer thicknesses is large, allowing the appearance of vortices in all four corners of the cavity, the number of these vortices decreases as this ratio diminishes. When the ratio approaches 1, the flow-separated structure no longer emerges. This phenomenon is independent of the absolute value of δ_u, considering solely the relative size of δ_x and δ_y. Indeed, a greater discrepancy between δ_x and δ_y leads to a more pronounced curvature of the boundary layer as it turns in the corner, rendering it more susceptible to the formation of a vortex. This finding provides a new perspective on understanding the flow separation phenomenon of low-Pr fluids under a weak nonlinear or laminar regime.

C. Wall effects on the global transport

The normalized global heat and momentum transport for different wall conductance ratios are depicted in Fig. 17. The calculated $(\mathrm{Nu}_B - 1)/(\mathrm{Nu}_0 - 1)$ can be formulated as a function of $\mathrm{Ha}/\mathrm{Gr}^{1/3}$, a ratio derived from the Lorentz force term in the modified momentum equation:

$$\frac{d\boldsymbol{u}^*}{dt^*} = -\nabla^* p^* - \mathrm{Pr}\nabla^{*2}\boldsymbol{u}^* + \mathrm{Pr}T^* e_y - \mathrm{Pr}\mathrm{Ha}^2\mathrm{Ra}^{-\frac{2}{3}}(\boldsymbol{j}^* \times \boldsymbol{B}^*). \tag{16}$$

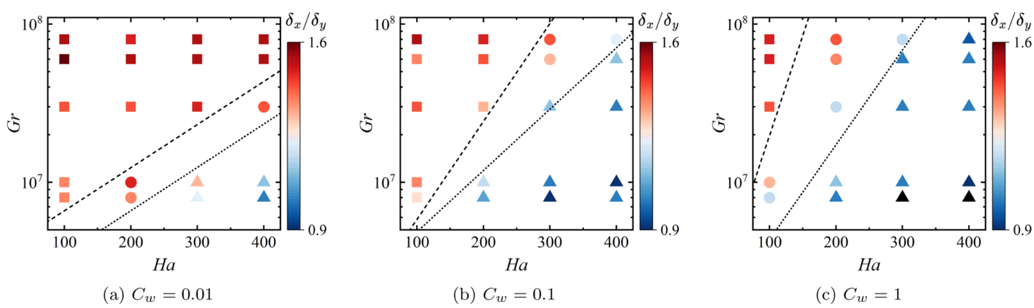

FIG. 16. Phase diagram representing the corner vortex morphology in the cavity at each parameter. Squares represent the presence of four corner vortices, circles denote only two vortices, lower left and upper right, and triangles signify the absence of vortices. The symbols are colored by the ratio of the thickness of the horizontal and vertical boundary layers.

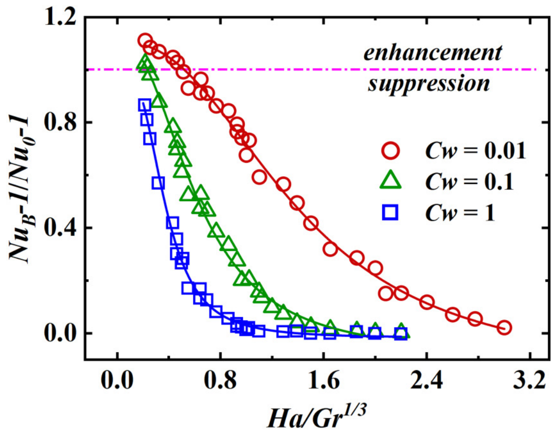

(a)

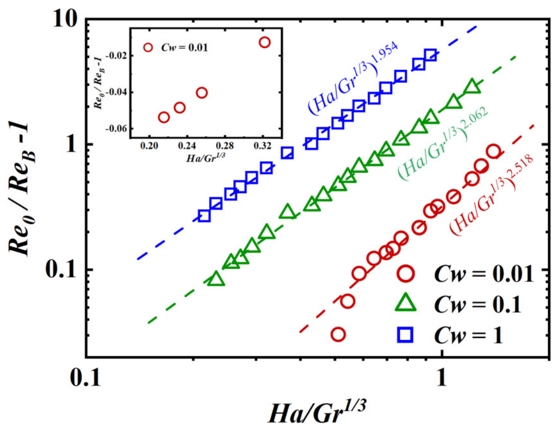

(b)

FIG. 17. Normalized global heat and momentum transports as functions of the control parameter $\mathrm{Ha/Gr}^{1/3}$.

The difference between Eqs. (16) and (2) is the selection of the characteristic length as $\mathrm{Ra}^{-1/3}L$, leading to the actual Rayleigh number of 1. This specific value reflects a critical state between conduction and convection. By adopting this characteristic length, the coefficients in front of the original buoyancy term are normalized, and Ra is effectively integrated into the Lorentz force term alongside Ha, thereby highlighting the interplay between the magnetic field and buoyancy-driven convection. A further simplification of $\mathrm{PrHa}^2\mathrm{Ra}^{-2/3}$ yields $\mathrm{Pr}^{1/3}(\mathrm{Ha/Gr}^{1/3})^2$. Given that conducting walls affect current distribution more directly compared to insulating walls, we have extended the applicability of $\mathrm{Ha/Gr}^{1/3}$ to describe heat transfer rates. The universal scaling behavior,

$$\frac{\mathrm{Nu}_B - 1}{\mathrm{Nu}_0 - 1} = a + \frac{b}{[1 + (c\mathrm{Ha/Gr}^{1/3})^n]}, \tag{17}$$

is supported by our data. The values of the parameters at different conductance ratios are shown in Table II. The rigid lines displayed in Fig. 17(a) exhibit an excellent fit to data groups for various conductance ratios.

In Fig. 17(a), dashed lines demarcate the parameters where the magnetic field impacts heat transfer efficiency positively and negatively. Notably, for $C_w = 0.01$ and 0.1, specific intervals exist

TABLE II. Parameter values for the universal scaling law, Eq. (17), at different values of C_w.

C_w	a	b	c	n
0.01	−0.156	1.263	0.715	2.406
0.1	−0.088	1.202	1.616	2.329
1	−0.017	1.035	2.731	3.016

where $(\mathrm{Nu}_B - 1)/(\mathrm{Nu}_0 - 1) > 1$, while this phenomenon is absent for $C_w = 1$. This nonmonotonic variation of the Nusselt number with increasing magnetic field was observed similarly in earlier studies on MHD natural convection [47]. Tagawa and Ozoe [48] provided a theoretical justification for this flow-rectifying effect in terms of the current distribution combined with the Lorentz force, arguing that this effect "increase the heat transfer rate due to the smooth flow." Furthermore, analyzing the flow field in Sec. III A unveils that low-conducting walls experience a transition from three-dimensional to quasi-two-dimensional behavior as the magnetic field intensifies. This process is marked by the inverse energy cascade, attenuating the small-scale, three-dimensional flow to sustain system-scale flow. The rectification effect gains more energy than what Joule damping dissipates, thereby bolstering convection and elevating jet velocity. Conversely, for highly conducting walls, the altered current distribution renders the response to the magnetic field highly sensitive. The augmented Lorentz force prompts the flow to attain a state close to Q2D even at minimal magnetic field strengths. During this phase, Hartmann braking emerges as the dominant magnetic damping mechanism. Specifically, the dissipation of the main vortex energy through boundary layer friction operates on the timescale $\tau_H = \frac{H}{2B}\sqrt{\frac{\rho}{\sigma\nu}}$, significantly surpassing the timescale $\tau_J = \frac{\rho}{\sigma B^2}$ of Joule damping. Consequently, Hartmann braking in the quasi-two-dimensional flow is much weaker than Joule dissipation in the three-dimensional flow. However, at this juncture, further increments in the magnetic field cease to enhance flow coherence. Under the escalating magnetic damping effect, flow strength can only decay monotonically, with no observed interval of heat transfer augmentation.

Nonetheless, an unresolved question concerns the exact process by which enhanced flow intensity and coherence contribute to increased heat transfer efficiency in the system. Prior research indicates that augmenting either the shear rate appropriately or increasing plume coverage can amplify the system's heat transfer rate. Jin [49] posited that the application of external shear could strengthen the LSC and facilitate interaction with secondary flows within the cavity. Huang *et al.* [50] and Chong *et al.* [8] reported that plume coherency and the condensation of coherent structures can be promoted through suitable geometric constraints. In addition to constrained RBC, research involving inclined convection and thermal convection with rough boundaries has verified that increasing plume coverage stands as a pivotal factor in enhancing heat transfer.

We seek to comprehend the roles played by wall shear and large-scale convective vortex (self-organizing plumes) in the heat transport process. To begin with, examining the impact of wall shear, snapshots portraying the heat flux $q = -\frac{\partial T}{\partial x}$ and shear stress $\tau_f = \sqrt{(\frac{\partial v}{\partial x})^2 + (\frac{\partial w}{\partial x})^2}$ at the heated wall $x = 0.5$ are illustrated in Figs. 18(a) and 18(b). Take note of the comparison in the distribution of brightly colored regions representing local peaks. Also plotted in Fig. 19(a) are the Nusselt number and the mean shear rate as a function of different conductivity at $\mathrm{Gr} = 1 \times 10^8$, $\mathrm{Ha} = 100$, normalized by the value of no magnetic field.

The snapshots exhibit very similar instantaneous field structures, and both the Nu and mean shear rate display consistent patterns. However, it might be premature to assert that increasing the wall shear definitively enhances the overall heat transfer. A meticulous comparison of the bright patches on the snapshots provides some further intuition. The counterclockwise rotation of the primary convective vortex induces a horizontal cold flow close to the bottom, directly impacting the hot wall, and generating an intense local heat flux—referred to as the "impact region." Above the impact region lies the "shear region," formed by the vertical wind of the LSC sweeping over the hot wall. Further upwards, the fluid moves away from the hot wall due to geometrical constraint, and no

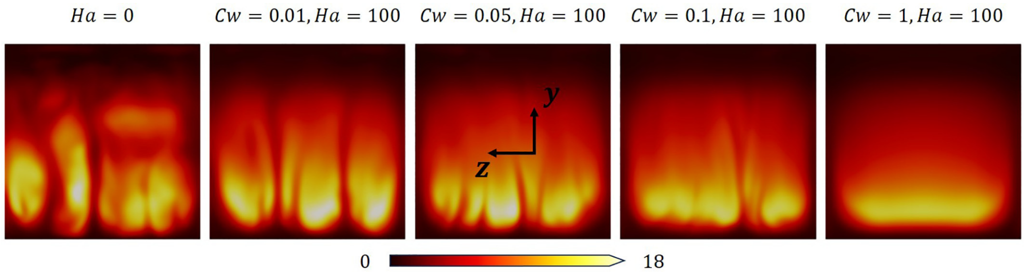

(a) Snapshot of local heat flux q at the heated wall $x = 0.5$

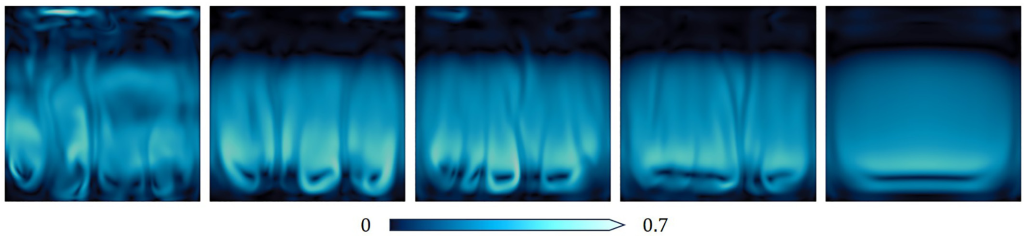

(b) Snapshot of local shear stress τ at the heated wall $x = 0.5$

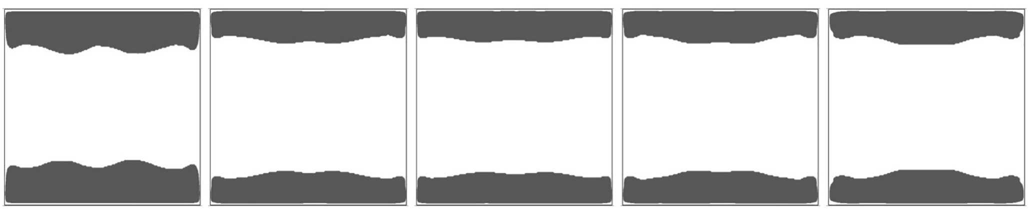

(c) Plume converage in the mid yz-plane $x = 0$ extracted from the mean field, marked in black

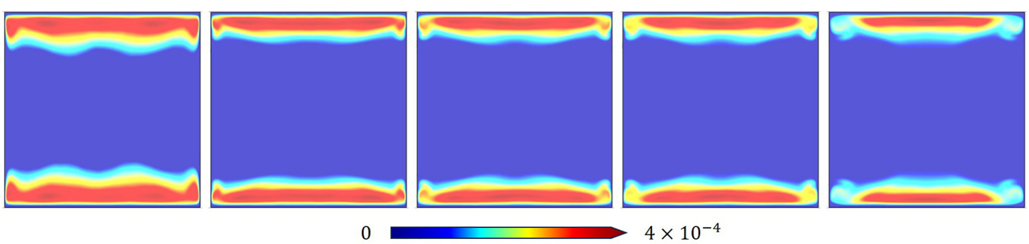

(d) Heat flux content Q_p contained within the plume region

FIG. 18. Cross-sections of various quantities at Gr $= 1 \times 10^8$. The parameters from left to right are as follows: Ha $= 0$; $C_w = 0.01$, Ha $= 100$; $C_w = 0.05$, Ha $= 100$; $C_w = 0.1$, Ha $= 100$; $C_w = 1$, Ha $= 100$.

additional plume emission is observed in the laminar or weakly chaotic state. Consequently, the local heat transfer exhibits a monotonic decrease in this direction. We note that in the impact region, the area exhibiting the highest heat flux (bright yellow) is typically accompanied by the lowest localized shear rate (black). Additional shear stress extremes emerge in the upper corner, but this region contributes little to the heat transfer, and it seems that strong shear does not correspond well to strong heat transfer.

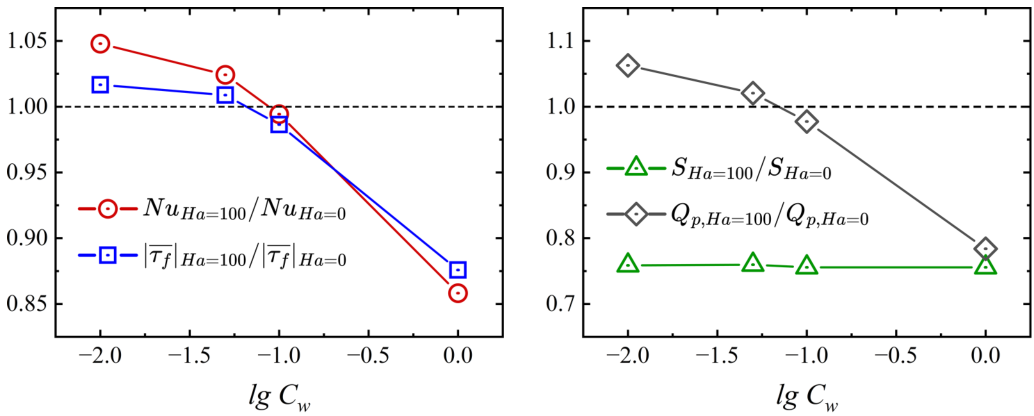

(a) Nusselt number and mean shear rates

(b) Plume area and heat flux content

FIG. 19. Statistics of dimensionless physical quantities related to heat transfer. The C_w corresponding to the parameter points in the figures are 0.01, 0.05, 0.1, and 1 from left to right, using a logarithmic treatment. (a) Volume-averaged Nusselt number $\mathrm{Nu}/\mathrm{Nu}_0$ and mean shear rate $|\overline{\tau_f}|/|\overline{\tau_f}|_0$ at the heated wall $x = 0.5$. (b) Plume area S/S_0 in the mid-yz plane extracted from the mean field and the actual heat flux content $Q_p/Q_{p,0}$ transported within the plume region.

The quantitative assessment of flow coherence relies on statistical plume coverage. We refer to Huang's definition [50] in RBC to establish a criterion applicable to vertical convection: $\sqrt{\mathrm{RaPr}}\ |u_x T| > \lambda \mathrm{Nu}$. It is required that the hot and cold plumes efficiently transport more heat flux in the horizontal direction. This stands in contrast to the temperature-based definition typically employed in RBC: $\pm(T - \langle T\rangle_{x,y}) > \lambda T_{\mathrm{rms}}$, which necessitates the cold (or hot) plume to be cooler (or hotter) than the surrounding fluid. Here, λ is an empirical parameter set at the value of $\lambda = 1$. The choice of the convection criterion is based on the fundamental disparity between VC and RBC: in vertical convection, heat transfer occurs horizontally, orthogonal to gravity's vertical direction. The simple upward and downward fluid movement driven solely by temperature differences fails to portray the intensity of horizontal heat transport. Additionally, the heat flux content within the plume-covered area has been quantified as a further assessment of flow coherence under magnetic fields ($Q_p = \int u_x T\, dS_{\mathrm{plume}}$, the ability of the plume to undertake heat transport). Figures 18(c), 18(d) and 19(b) depict the respective results of the time-averaged field at the central yz-plane. Observations reveal minimal alterations in the plume coverage following the magnetic field application, despite changes in conductivity. The ratio of the plume coverage to the area without the magnetic field remains approximately 0.76. However, the heat flux carried by almost the same area of the plume is quite different, and a smaller plume coverage than that of the magnetic-field-free case can take up a stronger convective transport, notably for $C_w = 0.01$ and 0.05. This suggests that the horizontal heat transport contributed by the plume per unit area (Q_p/S) can be increased by the rectification effect of the magnetic field in MHD vertical convection, essentially generating better self-organized and more energetic clusters of hot and cold plumes, which increases the degree of coherence of the global flow and thus improves the heat transfer efficiency. In this process, the alteration in wall shear is more a result of vertical winds sweeping across the sidewalls as the flow strength of the LSC increases. As Howland *et al.* [12] mentioned, the wall shear stress in VC is not predetermined but emerges as a responsive parameter within the system.

Except for Nu, the scaling behavior of Re is also estimated in Fig. 17(b). Here we adopt the definition based on the kinetic energy, $\mathrm{Re} = L\sqrt{\langle \boldsymbol{uu}\rangle}/\nu$, and $\langle\cdot\rangle$ denotes the averaging in time and volume. Referring to the empirical equations for Nu, we assume that the Reynolds number normalized by its reference value at $\mathrm{Ha} = 0$ satisfies a similar scaling relationship, $\mathrm{Re}_B/\mathrm{Re}_0 = 1/[1 + \alpha(\mathrm{Ha}/\mathrm{Gr}^{1/3})^{\beta}]$. So we plot $\mathrm{Re}_0/\mathrm{Re}_B - 1$ versus $\mathrm{Ha}/\mathrm{Gr}^{1/3}$ on a logarithmic scale, and all data collapse into a universal

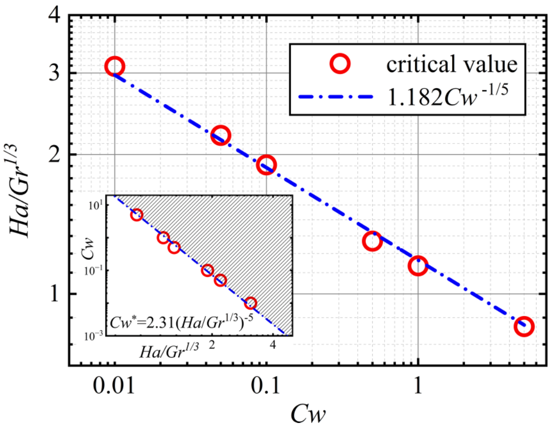

FIG. 20. The critical conditions to approach heat conduction for various wall conductance ratios. The inset represents the threshold C_w^* as a function of Ha and Gr. If $C_w > C_w^*$, heat transfer degenerates into thermal conduction, as shown in the shaded area.

power law, which can verify our assumption. The cases shown in Fig. 17(b) are the reduction of kinetic energy by an external magnetic field. But as shown in Fig. 17(a), when $C_w = 0.01$, the presence of a weak magnetic field enhances the main circulation and thus increases the heat transfer rate. This is also shown in the inset, where the increase in Re makes the result negative instead, which also proves that the variation trend of Nu and Re is consistent. A similar scaling behavior has also been confirmed for RBC in cylindrical cells [51].

In addition, we can establish that convection is entirely suppressed when $(\mathrm{Nu}_B - 1)/(\mathrm{Nu}_0 - 1) \rightarrow 0$, and heat transfer relies solely on heat conduction. Based on Fig. 20, we can infer that the critical values of $\mathrm{Ha}/\mathrm{Gr}^{1/3}$ for different conductive walls are proportional to $C_w^{-1/5}$. To ensure the universality of the data, we consider additional threshold conditions for C_w=0.05, 0.5, and 5. Remarkably, the points converge excellently with the straight line on the logarithmic plot. Upon reintegrating this scaling relation, we can derive a dimensionless parameter $C_w^{1/5}\mathrm{Ha}/\mathrm{Gr}^{1/3}$ representing the relative magnitude of the Lorentz force to the buoyancy force under the condition of conductive boundary, with 1.182 as the threshold for distinguishing between heat conduction and convection. Here the power exponent $1/5$ of C_w is a positive value less than unity, aligning with the fundamental physical principle that wall conductivity acts as positive feedback on the Lorentz force, but it cannot continue indefinitely, and the results will no longer change significantly after C_w increases to a certain value. Similarly, we can introduce critical C_w^* as a function of Ha and Gr: $C_w^* = 2.31(\mathrm{Ha}/\mathrm{Gr}^{1/3})^{-5}$. If $C_w > C_w^*$, the heat transfer degenerates into thermal conduction (shaded area in the inset of Fig. 20), and conversely, convection exists or even dominates. It should be emphasized that the above scaling is based on statistical results within the parameter range of this study, and all three independent parameters Ha, Gr, and C_w are significant. Even if their combination $C_w^{1/5}\mathrm{Ha}/\mathrm{Gr}^{1/3}$ is identical, it does not guarantee that the system will exhibit the same flow state.

IV. CONCLUSIONS

Through 3D numerical simulations, we have investigated the vertical convection of liquid metal in a cavity, with different magnetic field strengths and wall conductivities. Our primary objective was to elucidate the physical mechanisms that give rise to the wall effect on the flow and to provide a quantitative correlation between Nu, Re and Ha, Gr. The key findings, which address the research questions raised in the Introduction, are presented as follows.

For low-conducting walls, the flow visualization shows a transition to the Q2D state with an increasing magnetic field. Small-scale structures subject to main vortex entrainment develop into highly correlated side vortices along the field lines. System-scale structures acquire more energy from this ordering effect than is dissipated by magnetic damping. The flow intensity of the main roll increases at a certain range of magnetic field. However, for high-conducting walls, the current distribution within the side layers is essentially perpendicular to the magnetic field and features a greater current density, rendering the flow more susceptible to magnetic field variation. The feasibility of three-dimensional flow is markedly constrained, preventing further enhancement in flow coherence. Consequently, convection undergoes rapid attenuation due to Hartmann braking, which is also reflected in the flow topology. Considering that the steady flow at this state is dominated by the equilibrium between the Lorentz force and the buoyancy force, it can be deduced that the flow of the horizontal jet satisfies the scaling $Q_h = \mathrm{Gr}/6\mathrm{Ha}^2$ and agrees with the simulation results.

As the wall conductivity increases, the convection evolves from high-frequency, high-amplitude oscillation to lower-frequency, quasiperiodic oscillation, culminating in its complete suppression. The predominant frequency of these oscillations aligns with the vortex overturning frequency, underscoring the coherence of large-scale structures in vertical convection. The thermal stratification parameters within the core region exhibit nonmonotonic behavior. Furthermore, the development of corner vortices is intricately linked to the dynamics of the boundary layer. A more pronounced disparity between δ_x and δ_y intensifies the curvature of the boundary layer at the corners, thereby facilitating flow separation and recirculation.

The correlation function involving $\mathrm{Ha}/\mathrm{Gr}^{1/3}$ effectively models the average heat and momentum transfer coefficient, thus enabling an extension of the scaling behavior from insulating to conducting walls. The enhancement of convection observed in low-conducting walls is attributed to augmented flow coherence. Building upon the traditional understanding, where the condensation of coherent structures typically manifests as increased plume coverage, we find that in the unique context of a magnetic field, the flow's self-organization does not significantly alter the plume area S. Rather, it fosters the generation of more energetic clusters of hot and cold plumes, thereby elevating the horizontal heat transport per unit area of the plume Q_p/S. This process plays a pivotal role in the amplification of overall heat transfer efficiency.

[1] G. A. Glatzmaier and P. H. Roberts, A three-dimensional convective dynamo solution with rotating and finitely conducting inner core and mantle, Phys. Earth Planet. Inter. **91**, 63 (1995).

[2] K. Zhang and G. Schubert, Magnetohydrodynamics in rapidly rotating spherical systems, Annu. Rev. Fluid Mech. **32**, 409 (2000).

[3] D. H. Kelley and T. Weier, Fluid mechanics of liquid metal batteries, Appl. Mech. Rev. **70**, 020801 (2018).

[4] S. Smolentsev, Physical background, computations and practical issues of the magnetohydrodynamic pressure drop in a fusion liquid metal blanket, Fluids **6**, 110 (2021).

[5] B. Hof, A. Juel, and T. Mullin, Magnetohydrodynamic damping of convective flows in molten gallium, J. Fluid Mech. **482**, 163 (2003).

[6] G. Ahlers, S. Grossmann, and D. Lohse, Heat transfer and large scale dynamics in turbulent rayleigh-bénard convection, Rev. Mod. Phys. **81**, 503 (2009).

[7] K. Sugiyama, R. Ni, R. J. A. M. Stevens, T. S. Chan, S.-Q. Zhou, H.-D. Xi, C. Sun, S. Grossmann, K.-Q. Xia, and D. Lohse, Flow reversals in thermally driven turbulence, Phys. Rev. Lett. **105**, 034503 (2010).

[8] K. L. Chong, S.-D. Huang, M. Kaczorowski, K.-Q. Xia *et al.*, Condensation of coherent structures in turbulent flows, Phys. Rev. Lett. **115**, 264503 (2015).

[9] G. Batchelor, Heat transfer by free convection across a closed cavity between vertical boundaries at different temperatures, Q. Appl. Math. **12**, 209 (1954).

[10] F. Trias, M. Soria, A. Oliva, and C. Pérez-Segarra, Direct numerical simulations of two- and three-dimensional turbulent natural convection flows in a differentially heated cavity of aspect ratio 4, J. Fluid Mech. **586**, 259 (2007).

[11] L. Zwirner, M. S. Emran, F. Schindler, S. Singh, S. Eckert, T. Vogt, and O. Shishkina, Dynamics and length scales in vertical convection of liquid metals, J. Fluid Mech. **932**, A9 (2022).
[12] C. J. Howland, C. S. Ng, R. Verzicco, and D. Lohse, Boundary layers in turbulent vertical convection at high prandtl number, J. Fluid Mech. **930**, A32 (2022).
[13] K.-H. Kim, J. Ahn, and J.-I. Choi, Mean thermal energy balance analysis in differentially heated vertical channel flows, Phys. Fluids **33**, 065120 (2021).
[14] C. S. Ng, A. Ooi, D. Lohse, and D. Chung, Vertical natural convection: application of the unifying theory of thermal convection, J. Fluid Mech. **764**, 349 (2015).
[15] O. Shishkina, Momentum and heat transport scalings in laminar vertical convection, Phys. Rev. E **93**, 051102(R) (2016).
[16] E. S. C. Ching, Heat flux and wall shear stress in large-aspect-ratio turbulent vertical convection, Phys. Rev. Fluids **8**, L022601 (2023).
[17] P. A. Davidson, *An Introduction to Magnetohydrodynamics* (Cambridge University Press, Cambridge, 2002).
[18] T. Tagawa, G. Authié, and R. Moreau, Buoyant flow in long vertical enclosures in the presence of a strong horizontal magnetic field. part 1. fully-established flow, Eur. J. Mech. B **21**, 383 (2002).
[19] J. Sommeria and R. Moreau, Why, how, and when, mhd turbulence becomes two-dimensional, J. Fluid Mech. **118**, 507 (1982).
[20] W. K. Hussam, M. C. Thompson, and G. J. Sheard, Dynamics and heat transfer in a quasi-two-dimensional mhd flow past a circular cylinder in a duct at high hartmann number, Int. J. Heat Mass Transf. **54**, 1091 (2011).
[21] L. Chen, A. Pothérat, M. Ni, and R. J. Moreau, Direct numerical simulation of quasi-two-dimensional mhd turbulent shear flows, J. Fluid Mech. **915**, A130 (2021).
[22] L. Bühler, C. Mistrangelo, and S. Molokov, Validity of quasi-2d models for magneto-convection, Magnetohydrodynamics **51**, 321 (2015).
[23] J. Hunt, Magnetohydrodynamic flow in rectangular ducts, J. Fluid Mech. **21**, 577 (1965).
[24] T. Tagawa and H. Ozoe, The natural convection of liquid metal in a cubical enclosure with various electro-conductivities of the wall under the magnetic field, Int. J. Heat Mass Transf. **41**, 1917 (1998).
[25] I. Di Piazza and M. Ciofalo, Mhd free convection in a liquid-metal filled cubic enclosure. i. differential heating, Int. J. Heat Mass Transf. **45**, 1477 (2002).
[26] N. L. Gajbhiye and V. Eswaran, Mhd buoyant flow in a cubical enclosure at low to high hartmann number, Int. J. Therm. Sci. **134**, 168 (2018).
[27] Z. Jing, M.-J. Ni, and Z.-H. Wang, Numerical study of mhd natural convection of liquid metal with wall effects, Numer. Heat Transf. Pt. A **64**, 676 (2013).
[28] R. J. Singh and T. B. Gohil, The numerical analysis on the variation of electric potential, electric current and lorentz force with its influence on buoyancy-driven conjugate heat transfer and fluid flow using openfoam, Fusion Eng. Des. **148**, 111300 (2019).
[29] N. S. Bondareva and M. A. Sheremet, Natural convection heat transfer combined with melting process in a cubical cavity under the effects of uniform inclined magnetic field and local heat source, Int. J. Heat Mass Transf. **108**, 1057 (2017).
[30] S. Grossmann and D. Lohse, Scaling in thermal convection: a unifying theory, J. Fluid Mech. **407**, 27 (2000).
[31] T. Zürner, Refined mean field model of heat and momentum transfer in magnetoconvection, Phys. Fluids **32**, 107101 (2020).
[32] L. Chen, B.-Q. Liu, and M.-J. Ni, Study of natural convection in a heated cavity with magnetic fields normal to the main circulation, Int. J. Heat Mass Transf. **127**, 267 (2018).
[33] F. Sebilleau, R. Issa, S. Lardeau, and S. P. Walker, Direct numerical simulation of an air-filled differentially heated square cavity with rayleigh numbers up to 1011, Int. J. Heat Mass Transf. **123**, 297 (2018).
[34] A. Hudoba and S. Molokov, Linear stability of buoyant convective flow in a vertical channel with internal heat sources and a transverse magnetic field, Phys. Fluids **28**, 114103 (2016).

[35] M.-J. Ni, R. Munipalli, P. Huang, N. B. Morley, and M. A. Abdou, A current density conservative scheme for incompressible mhd flows at a low magnetic reynolds number. part ii: On an arbitrary collocated mesh, J. Comput. Phys. **227**, 205 (2007).

[36] M.-J. Ni, R. Munipalli, N. B. Morley, P. Huang, and M. A. Abdou, A current density conservative scheme for incompressible mhd flows at a low magnetic reynolds number. part i: On a rectangular collocated grid system, J. Comput. Phys. **227**, 174 (2007).

[37] L. Chen, S. Smolentsev, and M.-J. Ni, Toward full simulations for a liquid metal blanket: part 2. computations of mhd flows with volumetric heating for a pbli blanket prototype at ha 104 and gr 1012, Nucl. Fusion **62**, 026042 (2022).

[38] M. Ravi, R. Henkes, and C. Hoogendoorn, On the high-rayleigh-number structure of steady laminar natural-convection flow in a square enclosure, J. Fluid Mech. **262**, 325 (1994).

[39] N. T. Baker, A. Pothérat, L. Davoust, and F. Debray, Inverse and direct energy cascades in three-dimensional magnetohydrodynamic turbulence at low magnetic reynolds number, Phys. Rev. Lett. **120**, 224502 (2018).

[40] Z. L. Lim, K. L. Chong, G.-Y. Ding, and K.-Q. Xia, Quasistatic magnetoconvection: heat transport enhancement and boundary layer crossing, J. Fluid Mech. **870**, 519 (2019).

[41] T. Vogt, J.-C. Yang, F. Schindler, and S. Eckert, Free-fall velocities and heat transport enhancement in liquid metal magneto-convection, J. Fluid Mech. **915**, A68 (2021).

[42] G. K. Batchelor, Small-scale variation of convected quantities like temperature in turbulent fluid part 1. general discussion and the case of small conductivity, J. Fluid Mech. **5**, 113 (1959).

[43] T. Yanagisawa, Y. Hamano, T. Miyagoshi, Y. Yamagishi, Y. Tasaka, and Y. Takeda, Convection patterns in a liquid metal under an imposed horizontal magnetic field, Phys. Rev. E **88**, 063020 (2013).

[44] M. Akashi, T. Yanagisawa, Y. Tasaka, T. Vogt, Y. Murai, and S. Eckert, Transition from convection rolls to large-scale cellular structures in turbulent rayleigh-bénard convection in a liquid metal layer, Phys. Rev. Fluids **4**, 033501 (2019).

[45] Q. Wang, H.-R. Liu, R. Verzicco, O. Shishkina, and D. Lohse, Regime transitions in thermally driven high-rayleigh number vertical convection, J. Fluid Mech. **917**, A6 (2021).

[46] W. Xu, Y. Wang, X. He, X. Wang, J. Schumacher, S.-D. Huang, and P. Tong, Mean velocity and temperature profiles in turbulent rayleigh-bénard convection at low prandtl numbers, J. Fluid Mech. **918**, A1 (2021).

[47] K. Okada and H. Ozoe, Experimental heat transfer rates of natural convection of molten gallium suppressed under an external magnetic field in either the x, y, or z direction, J. Heat Transf. **114**, 107 (1992).

[48] T. Tagawa and H. Ozoe, Enhancement of heat transfer rate by application of a static magnetic field during natural convection of liquid metal in a cube, J. Heat Transf. **119**, 265 (1997).

[49] T.-C. Jin, J.-Z. Wu, Y.-Z. Zhang, Y.-L. Liu, and Q. Zhou, Shear-induced modulation on thermal convection over rough plates, J. Fluid Mech. **936**, A28 (2022).

[50] S.-D. Huang, M. Kaczorowski, R. Ni, and K.-Q. Xia, Confinement-induced heat-transport enhancement in turbulent thermal convection, Phys. Rev. Lett. **111**, 104501 (2013).

[51] R. Akhmedagaev, O. Zikanov, D. Krasnov, and J. Schumacher, Turbulent rayleigh–bénard convection in a strong vertical magnetic field, J. Fluid Mech. **895**, R4 (2020).